Chemical Engineering Journal 415 (2021) 128957

Contents lists available at ScienceDirect

Chemical Engineering Journal

journal homepage: www.elsevier.com/locate/cej

Protective effect of lipoic acid modification on brain dysfunctions of mice induced by mesoporous silica nanoparticles

Ailing Sun [a], Di Qian [a], Zheng Wang [a], Yiliang Xu [b], Haihong Ye [b,*], Chen-Jie Fang [a,*], Chun-Hua Yan [c]

[a] School of Pharmaceutics, Capital Medical University, Beijing 100069, China
[b] Department of Medical Genetics and Developmental Biology, School of Basic Medical Sciences, Beijing Key Laboratory of Neural Regeneration and Repair, Capital Medical University, Beijing 100069, China
[c] Beijing National Laboratory for Molecular Sciences, State Key Laboratory of Rare Earth Materials Chemistry and Applications & PKU-HKU Joint Laboratory on Rare Earth Materials and Bioinorganic Chemistry, Peking University, Beijing 100871, China

ARTICLE INFO

Keywords:
Mesoporous silica nanoparticles
Lipoic acid
Oxidative stress
Signaling pathway
Sociability decline
Cognition impairment

ABSTRACT

Mesoporous silica nanoparticles (MSNs) have shown potential in biomedicine due to their structural advantages. However, little is known concerning their ability crossing blood-brain barrier (BBB), and potential adverse effects on the brain function associated with MSNs exposure and counterpart solution remains to be elucidated. The findings in the present study indicate that pristine MSNs destroy BBB and enter into the brain, and therefore, the brain functions such as social ability and cognition of the mice is impaired remarkably. The *in vitro* study indicates that the pristine MSNs inhibit cellular proliferation via generation of reactive oxygen species (ROS), which results in impaired mitochondrial function and activates cellular apoptosis via JNK and p38 MAPK (mitogen-activated protein kinase) signaling pathway. The *in vivo* study demonstrates that exposure to the MSNs triggers oxidative stress, activates mitochondrial apoptosis signaling pathways and the caspase family, and leads to cell apoptosis in the brain. The mitigated damages both *in vitro* and *in vivo* are observed after exposure to lipoic acid (LA) modified MSNs (MSN-LA). The integrated multilevel toxicity assessments also indicate that the brain dysfunction may be mitigated by the modification of LA, due to superior antioxidative property of LA.

1. Introduction

With unique physicochemical features and properties, mesoporous silica have emerged as an excellent nanocarrier in biomedical application in the treatment of cancer and other diseases [1–8], even some silica particles have entered preclinical development stage as targeted cancer therapeutic agent [9]. Such a wide application of mesoporous silica in the pharmaceutical development has raised concern with the undesirable effect on biological system [10–19]. However, there is little information about the potential hazards of mesoporous silica to the brain and function, and their safety is still an urgent problem to be solved [20].

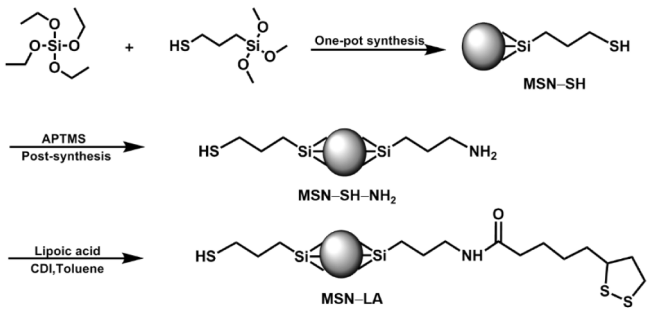
The previous studies have shown that the damage is mainly caused by oxidative stress (OS), due to abundant silanol group on the surface of the silica [21,22]. The OS results in oxidative damage to the lipids, proteins, and nucleic acids, which causes dysfunction of mitochondria and collapse of cellular energy system and eventually leads to cellular apoptosis [19,23]. The damage and decline of mitochondrial function accumulate in the brain and central nervous system (CNS), giving rise to impaired neurological function, memory loss and cognitive dysfunction [24–26]. In our previous work, transferrin (Tf) modified mesoporous silica MSN-Tf seemed to enter the brain, however, no evidence proved the ability of the pristine mesoporous silica to cross blood–brain barrier (BBB) [27]. Therefore, the safety of mesoporous silica, especially their effect on the BBB and brain function/behavior still needs to be studied.

As an antioxidant naturally found in mitochondria, lipoic acid (LA) has superior antioxidative property [28,29]. LA and its reduced form of dihydrolipoic acid (DHLA) can remove free radicals that cause disease and aging, modulate redox cycle, and decrease the level of lipid peroxidation in nervous cells to play a neuroprotective role [30–36]. Most importantly, as an important mitochondrial cofactor, LA can inhibit mitochondrial aging and mitochondrial dysfunction caused by the OS and improve neurological impairments including memory loss and cognitive dysfunction [37–44].

Surface modification is a powerful tool to alter the property and

* Corresponding authors.
E-mail addresses: yehh@ccmu.edu.cn (H. Ye), cjfang@ccmu.edu.cn (C.-J. Fang).

https://doi.org/10.1016/j.cej.2021.128957
Received 12 September 2020; Received in revised form 5 January 2021; Accepted 8 February 2021
Available online 13 February 2021
1385-8947/© 2021 Elsevier B.V. All rights reserved.



Scheme 1. Synthetic of MSN–SH and MSN–LA.

function of silica particles [45,46]. In this respect, LA modified mesoporous silica (MSN–LA, Scheme 1) was designed for the purpose to alleviate oxidative damage induced by the silanol. For comparison, the thiol modified MSNs (MSN–SH) with equivalent thiol content to that in MSN–LA was also fabricated. The cytotoxicity of these silica and their effect on the BBB and brain function/behavior of animals were explored *in vitro* and *in vivo*. Furthermore, the molecular mechanism of the cytotoxicity was revealed via the ROS generation and related signaling pathway analysis *in vitro* and ex vivo.

2. Materials and methods

2.1. Synthesis of mesoporous silica

The pristine mesoporous silica nanoparticles MSNs and sulfhydryl modified nanoparticles MSN–SH were synthesized with a modified co-condensation method [47–49]. LA modified nanoparticles MSN–LA was synthesized with a post-grafting and subsequently amide reaction [50–51]. The content of the thiol on the MSNs was measured with Ellman agent. The detailed measurement was based on the product instructions from Thermo Scientific Company.

2.2. Cytotoxicity bioassay

The cytotoxicity was examined with a standard MTT assay. Human SH-SY5Y neuroblastoma cells were cultured in DMEM media containing 10% FBS at 37 °C in an atmosphere of 5% CO_2. Then the cells were plated into a 96-well plate at a density of 5×10^3 cells per well and further treated with the nanoparticles at different concentrations. The absorbance was measured at 490 nm using a microplate reader (BIO-RAD, Model1680).

2.3. Detection of intracellular ROS

The cells were plated at a density of 1×10^5 cells per well. After treated with the nanoparticles (100 μg mL^{-1}) for 12 h, the cells were positioned on the UltraVIEW VoX spin disk confocal microscopy. DCFH-DA probe at a final concentration of 10 μM was added to the laser confocal dish. The fluorescence was qualitatively detected with spin disk confocal microscopy (PerkinElmer, UltraVIEW VoX, $\lambda_{Ex}/\lambda_{Em}$ = 488/525 nm). The quantitative detection was carried out with flow cytometer (BD, LSRFortessa SORP, $\lambda_{Ex}/\lambda_{Em}$ = 488/525 nm).

2.4. Mitochondrial assessment

For the morphology observation, the cells were plated into a laser confocal dish at a density of 1×10^5 cells per well. After treated with the nanoparticles (100 μg mL^{-1}) for 12 h, the cells were incubated with Mito tracker™ Red CMXRos fluorescent probe. Afterward, the cells were observed with STED ultra-high resolution confocal microscope (Leica, TCS SP8, $\lambda_{Ex}/\lambda_{Em}$ = 579/600 nm). For the measurement of mitochondrial membrane potential, the cells were plated into a 6-well plate at a density of 2×10^5 cells per well. After treated with the nanoparticles (100 μg mL^{-1}) for 12 h, the cells were incubated with JC-1 staining solution (5 μg mL^{-1}) for 20 min at 37 °C and rinsed twice with JC-1 staining buffer. The fluorescence was detected with the flow cytometer. The fluorescent intensity of JC-1 monomer was detected with $\lambda_{Ex}/\lambda_{Em}$ = 514/529 nm while that of the JC-1 polymer was detected with $\lambda_{Ex}/\lambda_{Em}$ = 585/590 nm. The mitochondrial function was analyzed with Seahorse XFe24 Analyser. The cells were plated into a XFe 24-well microplate at a density of 8×10^3 cells per well and treated with the nanoparticles (100 μg mL^{-1}) for 12 h. The analysis procedure for mitochondrial stress test was followed as the manufacturer instruction (Agilent). The basal oxygen consumption rate (OCR) and the OCR after drug injection (0.5 μM oligomycin, 4 μM FCCP and 0.5 μM rotenone) were measured. The presented data were normalized based on the cells counted with trypsinization.

2.5. Annexin V-FITC/PI staining

The cells were plated into a 6-well plate at a density of 2×10^5 cells per well. After treated with the nanoparticles (100 μg mL^{-1}) for 12 h, the cells were trypsinized, collected, and dispersed with 0.5 mL binding buffer. 5 μL of Annexin FITC and 5 μL of PI were added and incubated at room temperature in dark for 15 min. The cells were detected with the BD LSRFortessa flow cytometer with at a wavelength of 488 nm.

2.6. Western blot analysis

The cells were plated into a 6-well plate at a density of 2×10^5 cells per well. After treated with the nanoparticles (100 μg mL^{-1}) for 12 h, the cells were lysed in ice-cold and centrifuged, and the supernatants were collected. The protein concentrations of the extracts were determined by using the bicinchoninic acid (BCA) protein assay. The proteins were analyzed with western blot analysis in accordance with the standard procedure. Briefly, the proteins were separated by using 8% SDS polyacrylamide gel electrophoresis and incubated with antibodies P-JNK (abcam, ab124956, 1:1000), and P-p38 (abcam, ab178867, 1:1000) in 5% BSA/TBS/0.2%Tween at 4 °C overnight, respectively. The chemiluminescent reaction was performed with Super Signal West Dura Reagent (Pierce, Rockford), and blots were visualized with Fluor-S-Imager using Quantity One V4.1 software (BioRad, Hercules).

2.7. Blood-brain barrier (BBB) integrity test

The evans blue (EB) extravasation assay was performed as previously described [22,52]. Briefly, the mice were injected with EB dye (2% in saline, 8 mL kg^{-1}) via the tail vein. After for 1 h, the mice were sacrificed and perfused with saline through the coronary artery until the fluid from the right atrium became colorless. After decapitation, the brain was dissected, weighed, and photographed. Each brain was then incubated with formamide at 55 °C for 24 h. The supernatant was separated after centrifugation and the absorbance of EB supernatant was measured at 635 nm with a UV–Vis spectrophotometry. The brains dissected were processed by routine section and hematoxilin and eosin (H&E) staining to observe the physiological changes of the brain tissue. The slices were stained with H&E according to the standard procedure [53]. The eosin imparts a pink to red color to cytoplasm, and the hematoxylin stains the nucleus blue. The slices were observed and photographed with a Fully Automatic Slice Scanning System (Pannoramic scan).

2.8. Immunofluorescence (IF) experiments

The brain slices were fixed, permeabilized and blocked. The slices were then incubated with anti-Cytochrome *C* (abcam, ab133504, 1:200), anti-Caspase 9 (abcam, ab32539, 1:50), anti-Caspase 3 (CST, Asp175, 1:400), anti-P-JNK (abcam, ab124956, 1:100), and anti-P-p38 (abcam, ab178867, 1:500) at 4 °C for 12 h. The slices were incubated

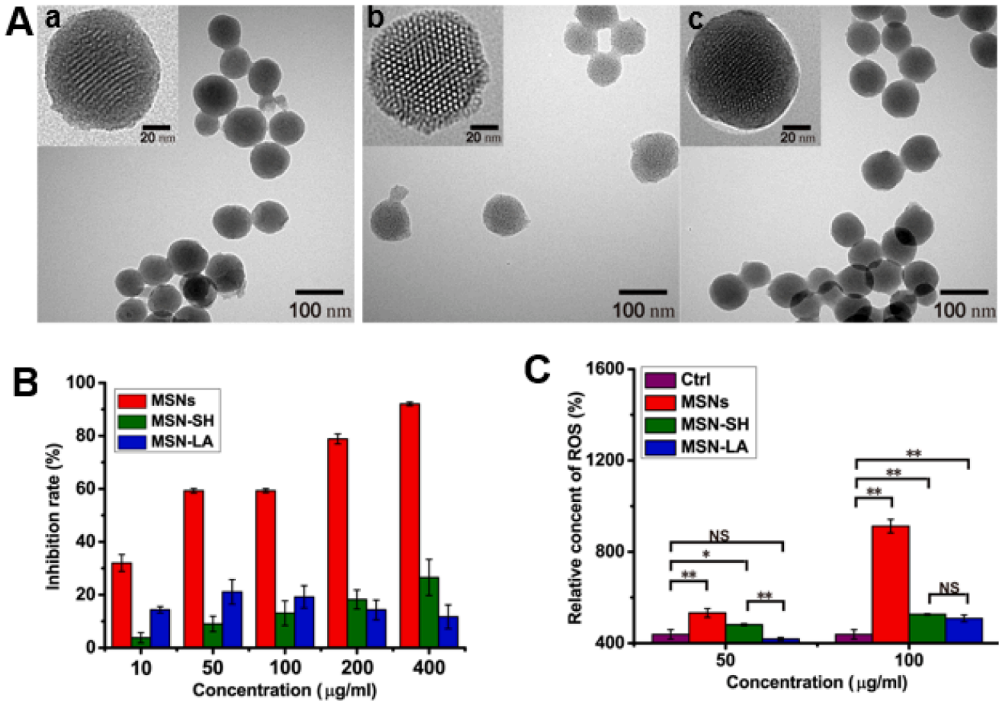


Fig. 1. (A) The TEM images of (a) MSNs, (b) MSN–SH, and (c) MSN–LA. (B) The inhibition profile of the mesoporous silica on SH-SY5Y cells after incubation for 24 h. (C) The intracellular ROS levels after incubation with the mesoporous silica. NS $p > 0.05$, * $p < 0.05$, ** $p < 0.01$. Scale bar, 100 μm.

with goat anti-rabbit secondary antibody at room temperature for 2 h. The slices were incubated with DAPI (5 μg mL^{-1}) for 10 min and sealed with an Anti-fluorescent-quenching sealant. Finally, the slices were observed and photographed on an Upright laser confocal microscope (Leica, TCS SP8).

2.9. The behavior test

The three-chambered social test and the novel object recognition test were constructed according to reported procedure [54,55]. During the experiments, the room environment was set up to minimize visual, olfactory, and auditory cues.

Mice were injected with the silica suspension in sterile 5% glucose at 25 mg kg^{-1} once a day via the tail vein for 14 days. The control mice were injected with sterile 5% glucose once a day via the tail vein for 14 days. From the 15th day to 20th day, the behavior of the mice was assessed with the three-chambered social interaction test and the novel object recognition test.

2.9.1. The three-chambered social test

The subject mice were habituated to the test room of three-chambered communicator for 20 min prior to start to the behavioral tasks in the first two days. On the following three days, the time course for social approach behaviour was recorded and analyzed. The subject mouse was placed in the middle chamber and acclimated to the environment for 5 min. After this habituation period, a strange mouse was placed inside a cage in one of the side chambers. An empty cage was placed in the opposite chamber. The mouse was then allowed to move freely throughout all three chambers over a 5-minute test session. Location of the stranger mouse and the empty cage was alternated between left and right chambers on consecutive sessions. The time of the subject mouse self-grooming (non-social behavior), sniffing the empty cage, and sniffing strange mice (social behavior) were recorded and measured.

2.9.2. The novel object recognition test

Three objects A, B, and C were applied in this test, where A and B is exactly the same and C is completely different. The two objects A and B were placed at the ends of the diagonal lines of the chamber. The subject mouse was placed into the chamber to familiarize with the environment for 5 min and then placed back into the feeding cage. After 1 h, the subject mouse was placed into the chamber again, while B object in the chamber was replaced with C object. The contact behavior between the mouse and two objects was recorded for 5 min. The mouse is considered to be sniffing the object when its nose is directed to the object and the distance between the nose tip and the object is 1 cm or less. The front paw on the object, the nose sniffing object, and licking object, etc. are all exploring objects, while posing a posture or climbing onto the object does not count as exploring objects.

3. Results and discussion

3.1. The synthesis and characterization

As shown in Fig. 1**A**, the obtained nanoparticles, including pristine mesoporous silica nanoparticles (MSNs), MSN–SH, and MSN–LA, are spherical in shape, with particle size of about 80 nm and regular porous structure. The content of thiol in both MSN–SH and MSN–LA was adjusted and measured to be 4.0 × 10^{-3} mol g^{-1}.

3.2. The cytotoxicity

The human neuroblastoma cell SH-SY5Y was selected as a cell model to explore the neurotoxicity of the obtained silica particles, as the SH-SY5Y cell line is characterized with catecholamine-like neurons and is widely used in neurobiology research [56,57]. The cytotoxicity of the mesoporous silica on the SH-SY5Y cell was examined with a standard 3-(4,5-dimethylthiazolyl-2)-2,5-diphenyltetrazolium bromide (MTT) assay **(**Fig. 1**B)**. The inhibitory rate of the pristine MSNs was the highest at every tested equivalent concentration, and the half inhibitory concentration (IC_{50}) was evaluated as 29.8 μg mL^{-1}. The cytotoxicity of MSN–SH and MSN–LA was significantly lowered, with inhibitory rate below 30% even at 400 μg mL^{-1}. The cytotoxicity of the pristine MSNs and MSN–SH is monotonously proportional to the nanoparticle

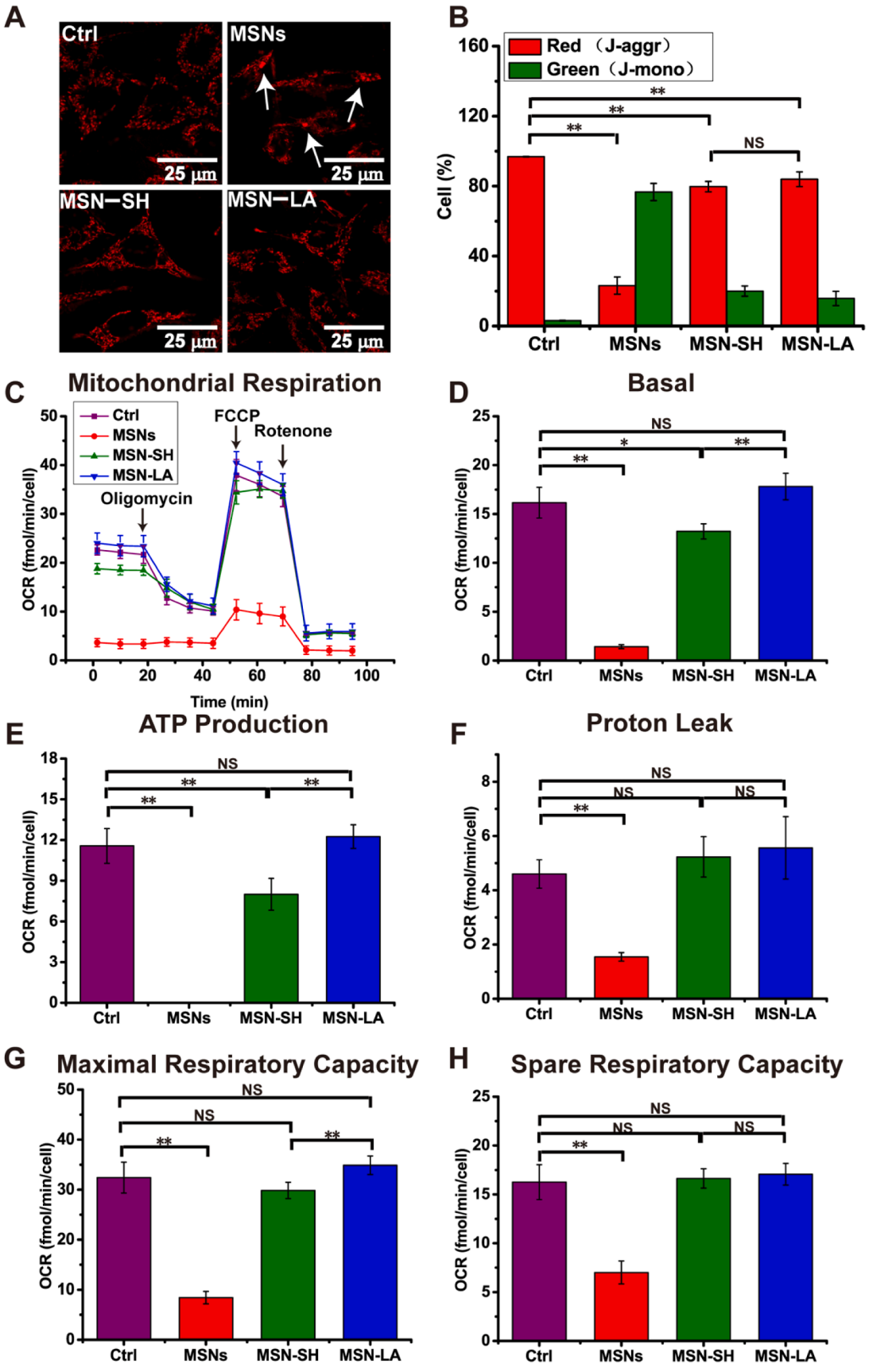


Fig. 2. The mitochondrial damage in SH-SY5Y cell after incubated with mesoporous silica for 12 h at 100 μg mL^{-1}. (A) The observed morphology of mitochondria. Scale bar, 25 μm. White arrows: the mitochondria swelled. (B) The mitochondrial membrane potential ($\Delta\psi_m$) measured with JC-1 staining. (C) Schematic analyzing of the mitochondrial function. (D) Basal oxygen consumption ratio (OCR). (E) OCR at ATP production. (F) OCR at proton leak stage. (G) OCR at mitochondrial maxima respiratory capacity. (H) OCR at mitochondrial spare respiratory capacity. NS $p > 0.05$, * $p < 0.05$, ** $p < 0.01$ as compared with control ($n = 4$).

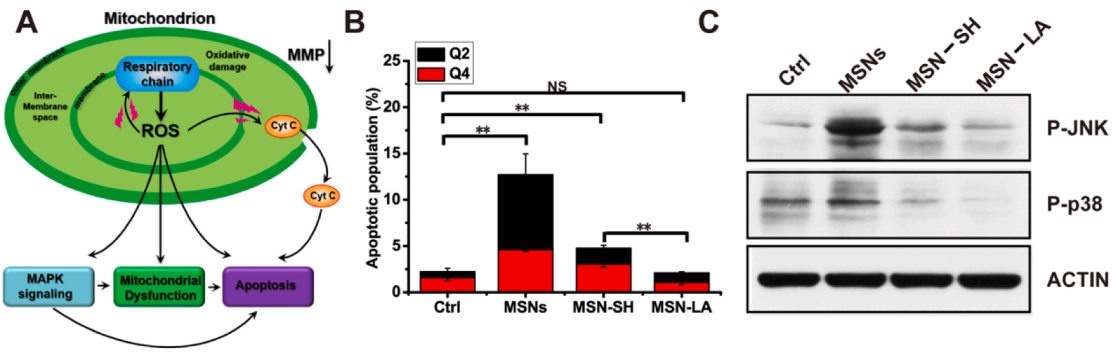


Fig. 3. The analysis of apoptosis and MAPK signaling pathway in SH-SY5Y cell after incubation with mesoporous silica for 12 h at 100 μg mL^{-1}. (A) Schematic diagram of the relationship between intracellular ROS and apoptosis through MAPK signaling. (B) The apoptotic population (%) of SH-SY5Y cell measured with flow cytometry. (C) Western blot analysis of phosphorylation levels of intracellular JNK and p38 protein in SH-SY5Y cells. NS $p > 0.05$, * $p < 0.05$, ** $p < 0.01$.

concentration. The MSN–LA showed the lowest cytotoxicity among the nanoparticles, with non-monotonous dependence on the nanoparticle concentration. Below the 100 μg mL^{-1} concentration, the inhibitory rate of MSN–LA against the SH-SY5Y cell proliferation increased with increased nanoparticle concentration. In contrast, the inhibitory rate decreased when the concentration of nanoparticle was higher than 100 μg mL^{-1}. It suggested that the high concentration of the MSN–LA may be beneficial to alleviation of the cytotoxicity induced by the mesoporous silica, due to the increased LA contents.

3.3. Intracellular ROS level

To explore the relationship between the cytotoxicity and the surface modification with thiol and LA, the intracellular ROS level was monitored qualitatively and quantitatively with spin disk confocal microscopy (SDCM, **Fig. S2**) and flow cytometry (FCM, Fig. 1**C**). For the pristine MSNs treated groups, statistically highly significant difference was observed between the groups treated at 50 and 100 μg mL^{-1}, suggesting the ROS generation in a concentration dependence manner. Among the groups treated with various nanoparticles at the same concentration, the fluorescent intensity (FI) in the pristine MSNs group was the strongest, indicating that the highest generation of intracellular ROS. After treated with the MSN–SH, the intracellular FI was significantly declined, indicating the lowered ROS generation. The weakest FI was observed in the group treated with the MSN–LA, indicating that intracellular ROS generation was the lowest. As the cytotoxicity was induced by the residual silanol, the oxidation resistant thiol group could alleviate the cytotoxicity through reducing intracellular ROS generation [58]. Interestingly, no statistically significant difference was observed between the control and the MSN–LA group at 50 ug mL^{-1}, implying that the MSN–LA might be safe at the low concentration.

3.4. The mitochondrial damage

The mitochondrial morphology was observed using Mito tracker™ Red CMXRos fluorescent probe. As shown in Fig. 2**A**, intracellular mitochondria are filamentous under normal conditions [59]. After treated with the pristine MSNs, the mitochondria swelled and became spotted or short rod-shaped [60,61], due to high level of ROS generated by the pristine MSNs. In contrast, no significant changes in cellular mitochondrial morphology were observed after treated with the MSN–SH and MSN–LA, due to the reductive property of thiol and LA.

The mitochondrial membrane potential (MMP, $\Delta\Psi_m$) was detected with the JC-1 probe after the treatment. As shown in Fig. 2**B&S3**, >90% of the cells in the control group showed red fluorescence. After treated with the pristine MSNs, the number of cells emitting red fluorescence was greatly decreased, but green increased, indicating that the MMP was significantly decreased. In the MSN–SH treated group, the number of the cells with reduced MMP was relatively small compared to the pristine MSNs group. The green fluorescent cells treated with MSN–LA were the least, suggesting the least decrease of the MMP among the various groups. The results revealed that the pristine MSNs induced the most severe damage to the mitochondria, with a significant reduced MMP. This is because a large amount of ROS is produced inside the cells after the treatment with the pristine MSNs. Due to the antioxidative ability of thiol and LA, the intracellular ROS generation was inhibited, and the loss of MMP was alleviated in the MSN–SH and MSN–LA groups, and thereby the damage to the mitochondria was weakened.

Because the mitochondria are known as cellular energetic factors for cell metabolism, we further explored the impact of various nanoparticles on mitochondrial metabolic and bioenergetic status, mainly the mitochondrial respiration and intracellular ATP level. The mitochondrial respiration was measured to quantify mitochondrial function by the oxygen consumption rate (OCR, fmol min^{-1} $cell^{-1}$). The OCR changes of the control and the treated SH-SY5Y cells upon addition of respiration modulators at the intervals are shown in Fig. 2**C**. The modulators include oligomycin, carbonyl cyanide 4-(trifluoromethoxy)phenylhydrazone (FCCP), and rotenone. Initially, treatment with the pristine MSNs caused a dramatic decrease in the basal OCR from 16.16 ± 1.57 fmol min^{-1} $cell^{-1}$ (the control) to 1.42 ± 0.21 fmol min^{-1} $cell^{-1}$ **(**Fig. 2**C&D)**. And then added oligomycin, an oxidative phosphorylation energy transfer inhibitor. Compared with the control, the MSNs treated cells displayed a prominent OCR decrease in ATP production from 11.46 ± 1.28 fmol min^{-1} $cell^{-1}$ (the control) to 0.00 ± 0.00 fmol min^{-1} $cell^{-1}$ (Fig. 2**E**). The pristine MSNs treatment also caused significant OCR changes at proton leak, indicating a declined proton leak (Fig. 2**F**). Further, a mitochondrial oxidative phosphorylation uncoupling agent FCCP is added, and then a dramatic decline (compared to the control) in the OCR peak of the maximal respiratory capacity rather than the rebound was observed (Fig. 2**C&G**), indicating the loss of spare respiratory capacity of the cell after treatment with the pristine MSNs [62]. Finally, rotenone was added that inhibits the complex enzyme I of the electron transport chain, so that the electron transfer from the NADPH to nicotinamide adenine dinucleotide (NADH) process is highly inhibited and the mitochondrial respiratory chain was shut down thoroughly, resulting in a steep decline in OCR peak of spare respiratory capacity both in the control and treated cells (Fig. 2**C&H**). The remaining OCR values represent nonmitochondrial O_2 consumption (Fig. 2**C**), including substrate oxidation and cell surface O_2 consumption [63,64]. It is observed that nonmitochondrial OCR in the MSNs treated cells is much less (1.96 ± 0.94 fmol min^{-1} $cell^{-1}$ than that in the control cells (5.51 ± 0.34 fmol min^{-1} $cell^{-1}$) (**Fig. S4**). These results suggest that both the mitochondrial respiration and nonmitochondrial respiration were effectively inhibited, contributing to the relatively superior cytotoxicity of the MSNs. Overall, the treatment with the pristine MSNs caused metabolic repression, as indicated with decreased basal OCR, lowered ATP

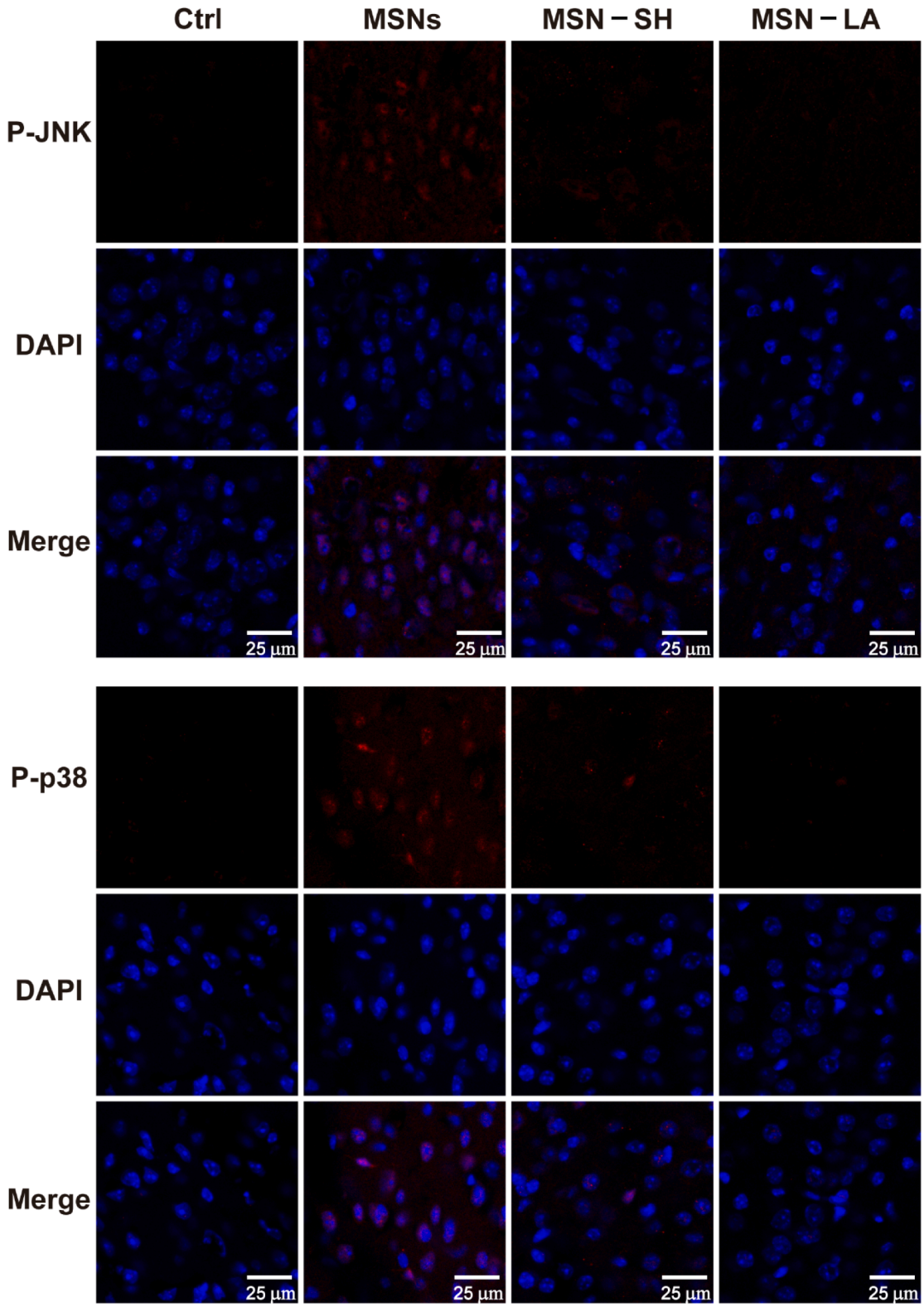


Fig. 4. Immunofluorescence analysis of relative phosphorylation of JNK and p38 in the MAPKs pathway in the brain slice of C57BL/6N mice. The nucleus was stained with 4′,6-diamidino-2-phenylindole (DAPI). Scale bar, 25 μm.

production, reduced proton leak, and inhibited nonmitochondrial respiration. It is noted that, however, MSN–SH and MSN–LA at the same concentrations made much less impact on the OCR than the pristine MSNs. In regard of the basal respiration, ATP production, proton leak, spare respiratory capacity, and maximal respiration, MSN–SH showed the slightest suppression and negligible change of the mitochondrial function and cellular energy systems because of the antioxidative capability of thiol and LA. The results proved obvious protective effect of MSN–LA on SH-SY5Y cells against ROS caused by the silanol of the silica nanoparticles.

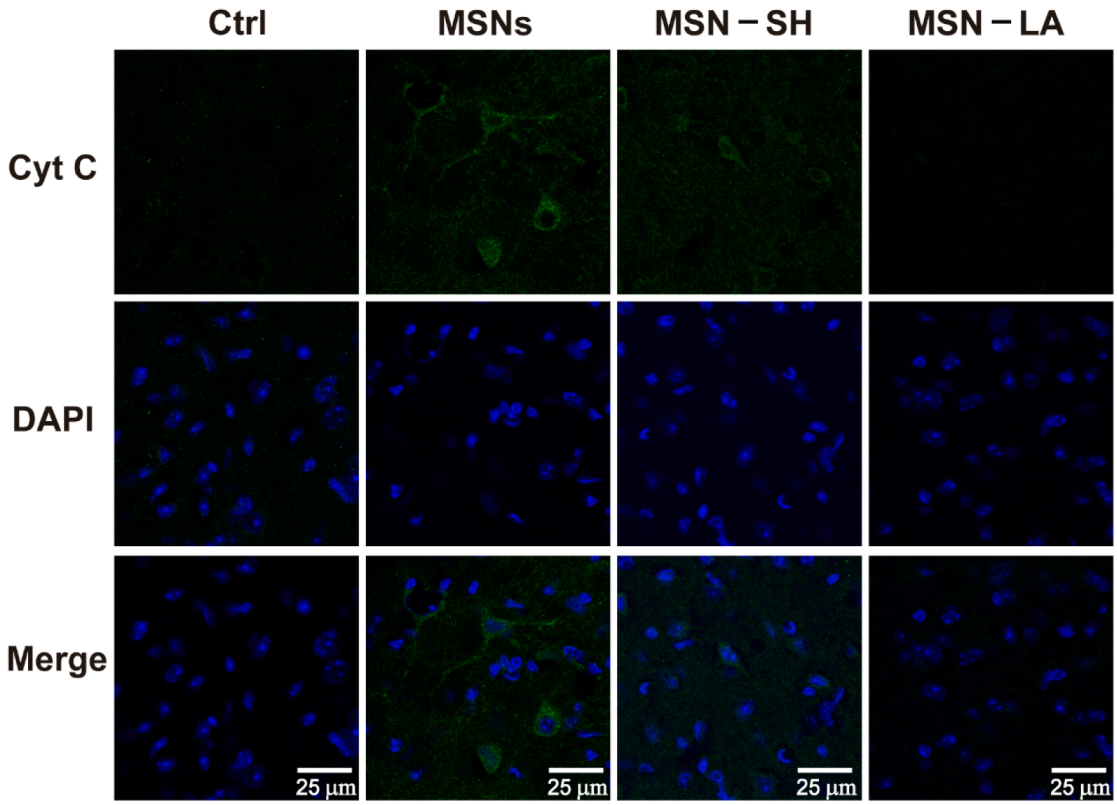


Fig. 5. Immunofluorescence analysis of the Cyt C release in the brain slice of C57BL/6N mice after exposure to the mesoporous silica. The nucleus was stained with DAPI, and Cyt C with Cytochrome *C* antibody. Scale bar, 25 μm.

3.5. In vitro apoptosis and MAPK (mitogen-activated protein kinase) signaling pathway

The loss of MMP is a significant event in the early stage of apoptosis (Fig. 3**A**) [65]. Accordingly, the apoptosis of the SH-SY5Y cells was detected with annex-V FITC/PI staining assay. As shown in Fig. 3**B**, the apoptotic rate of cells treated with the pristine MSNs is 12.70%, which is significantly increased compared with the control (2.24%). The apoptotic rate of the MSN–SH group declined to 4.76%, a 60% decrease compared with the pristine MSNs group. The apoptotic rate of the MSN–LA treated group decreased to only 2.10%, implying almost no impact on the apoptosis.

The MAPK signaling pathway is a cascade of multi-level protein kinases, including JNK and p38, which play important roles in cell cycle, cell proliferation, and apoptosis [66,67]. The inflammatory factors, tumor necrosis factors, and various stresses including radiation and oxidative damage can activate JNK and p38 signaling pathway to mediate cell apoptosis [68]. The activated JNK and p38 also trigger the intrinsic pathway, allowing Bcl-2 and Bcl-xl to participate in the release of the pro-apoptotic factor, cytochrome *C* (Cyt C), which in turn activates the caspase family and leads to apoptosis [69,70]. Therefore, the phosphorylation level of JNK and p38 protein in the treated SH-SY5Y cells was examined with Western blot analysis (Fig. 3**C**). The pristine MSNs caused the highest phosphorylation of JNK and p38 proteins, implying activated intrinsic pathways and apoptosis. When the cells were treated with the MSN–SH, the level of phosphorylation of JNK and p38 proteins increased only a little, while that in the MSN–LA group, no remarkable up-regulation was observed for the intracellular phosphorylated JNK and p38 proteins.

3.6. Ex vivo apoptotic signaling pathways

To further corroborate the MAPK signaling pathway in the animal brain, we used immunofluorescence staining to measure phosphorylation of JNK and p38 in the brain slice of C57BL/6N mice. As shown in Fig. 4, the pristine MSNs up-regulated the express of activated JNK and p38 proteins, indicating the MAPK signaling pathway was activated. In the MSN–SH and MSN–LA groups, phosphorylation levels of JNK and p38 proteins were decreased and negligible, compared with the pristine MSNs group. The lowest phosphorylation level was observed in the MSN–LA group, indicating that LA modification imposed more inhibitory effect on phosphorylation of JNK and p38 proteins **(Fig. S6)**. MSN–LA could reduce cellular apoptosis by suppressing the activation of the intrinsic apoptotic pathway to exert protective effects.

Activation of JNK and p38 signaling pathways promotes the release of Cyt C, activates intrinsic pathways, and thereby activates the caspase family and leads to apoptosis [65,71]. The caspase family plays an important role in the process of apoptosis [72]. As an initiator of the caspase activation, Caspase 9 is activated via binding to the aggregates formed by Cyt C and Apaf-1, and then it is clefted by various proteolytic enzymes and activates Caspase 3, the most deleterious apoptotic effector caspase [73,74]. Apoptosis becomes inevitable when Caspase 3 is activated.

As suggested by the *in vitro* study, the mesoporous silica induced ROS generation and mitochondrial damage and cellular apoptosis. Therefore, we examined the Cyt C release in the brain slice of C57BL/6N mice. As shown in Fig. 5***&S7***, intensive fluorescence signal from Cyt C was observed in the cytoplasm after treatment, indicating that the pristine MSNs promoted release of Cyt C. MSN–SH group showed weak but visible green fluorescence in cytoplasm, due to the reductive property of thiol on the surface of MSN–SH. In the MSN–LA group, no obvious fluorescence signal was observed, indicating Cyt C release was significantly reduced after LA exerted stronger antioxidative ability.

The release of Cyt C in turn caused the activation of Caspase 9 protein in the brain tissue, and ultimately led to activation of Caspase 3 and apoptosis **(**Fig. 6**)**. The strongest fluorescent signal represented for both

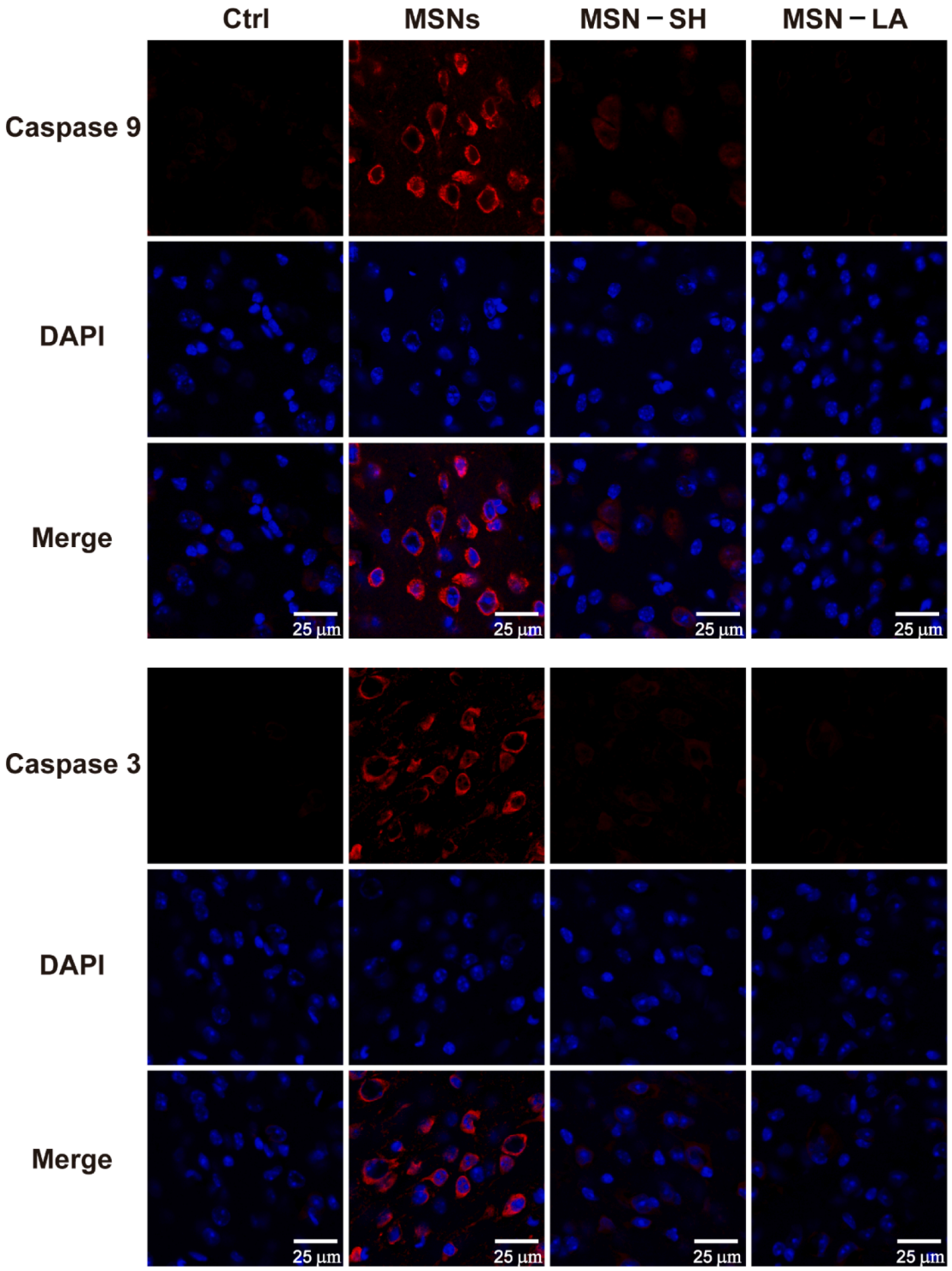


Fig. 6. Immunofluorescence analysis of Caspase 9 and Caspase 3 in the apoptotic signaling pathways in the brain slice of C57BL/6N mice after exposure to the mesoporous silica. The Caspase 9 and Caspase 3 were stained with Caspase 9 antibody and Caspase 3 antibody, respectively. Scale bar, 25 μm.

Caspase 9 and Caspase 3 was observed in the pristine MSNs group, followed by the MSN–SH group, whilst almost no fluorescent signal was visible in the MSN–LA group, indicating the level of Caspase 3 is the lowest and thus apoptosis is the slightest (**Fig. S8**). It suggests that the anti-oxidation and protective effects of LA modification are superior to those of thiol modification.

3.7. BBB integrity

The silica particles were administered to the C57BL/6N mice via the tail vein injection for consecutively 14 days at a dose of 25 mg kg^{-1} [13,22]. After treatment, the increase of the body weight of the mice in the pristine MSNs group was slower than that of the control group (p = 0.0000), suggesting a systemic acute toxicity (Fig. 7). In the MSN–SH and MSN–LA treated groups, the changes of mice body weight were not significant, compared with the control group, indicating that MSN–SH

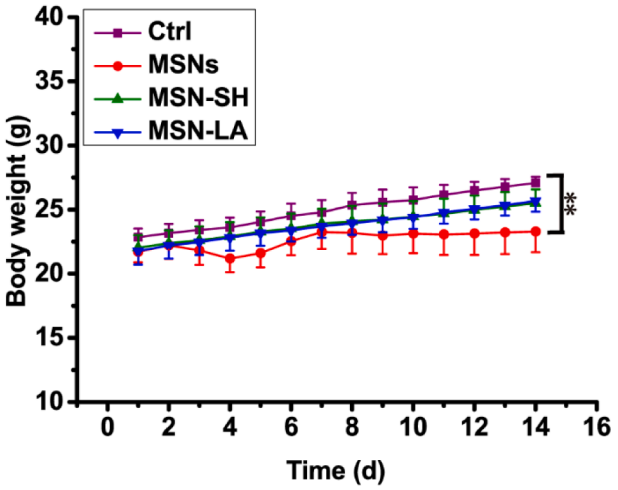


Fig. 7. The body weight changes of C57BL/6N mice after administration of mesoporous silica via the tail vein. n = 12.

and MSN–LA were less toxic and had little effect on the growth and development of the mice.

Although a few studies have hinted that spherical, rod-shaped nanoparticles could enter the brain [75], it is still not clear whether the mesoporous silica can cross the BBB. To observe the silica particles in the brain, mice brain slices were stained with hematoxylin-eosin (H&E) staining technique, in which the nuclei were stained blue-violet and the cytoplasm was stained red. As shown in Fig. 8, the silica particles agglomerated to various degrees were observed in the different parts of the brain, indicating that mesoporous silica were able to go across the BBB and enter into the brain [76].

Further, we used the dye Evans blue (EB) to evaluate the potential impact of MSNs on BBB permeability. The mice were sacrificed at day 21st, and EB extravasation assay was performed to quantify the dye into the brain (Fig. 9). The gross view of the mice brain showed that no obvious EB was observed in the control brain, while much more EB observed in the pristine MSNs treated mice brain. It suggests that the pristine MSNs broke the integrity of BBB and increased its permeability. It is noted that, however, the content of EB in the brain of the MSN–SH and the MSN–LA groups was much lower, even negligible in the MSN–LA group. This indicates that the integrity of the BBB was hardly disrupted, and the BBB function was relatively intact. Considering the large amount of ROS generated by the pristine MSNs *in vitro*, the pristine MSNs may cause damage of cerebral vascular endothelial cells so that it resulted in disturbance of BBB integrity and thereby went cross the BBB. Due to the antioxidative effect of thiol and LA modified on the MSN–SH and MSN–LA, much less ROS was generated, and much less damage was induced to the BBB.

3.8. Behavior tests

BBB represents a complex cellular gateway that regulates the transportation into the brain and CNS. BBB dysfunction is a hallmark of many neurodegenerative disorders such as Alzheimer's disease (AD). Changes in the BBB may associate with the process of impaired brain function, including cognitive decline, memory loss, and social behavioral disorders, etc. To explore the influence of the BBB disruption induced by the

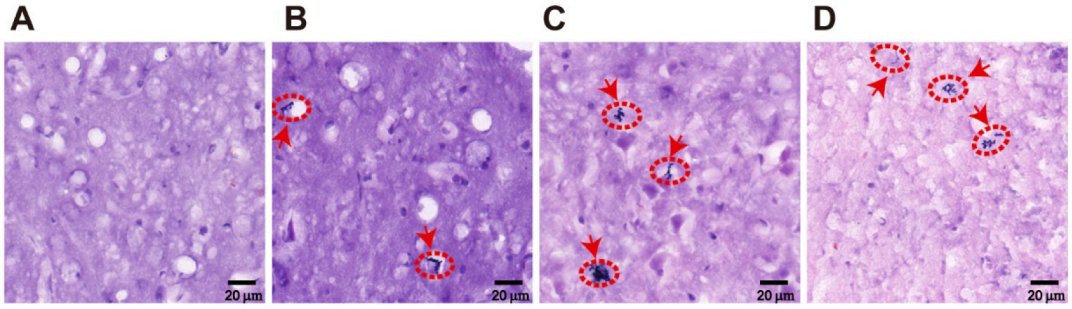


Fig. 8. H&E staining of C57BL/6N mice brain slices. The red arrows indicated the silica particles in the brain parenchyma across the BBB, as shown by red dotted circles. (A) the control, (B) pristine MSNs, (C) MSN–SH, and (D) MSN–LA groups. (For interpretation of the references to color in this figure legend, the reader is referred to the web version of this article.)

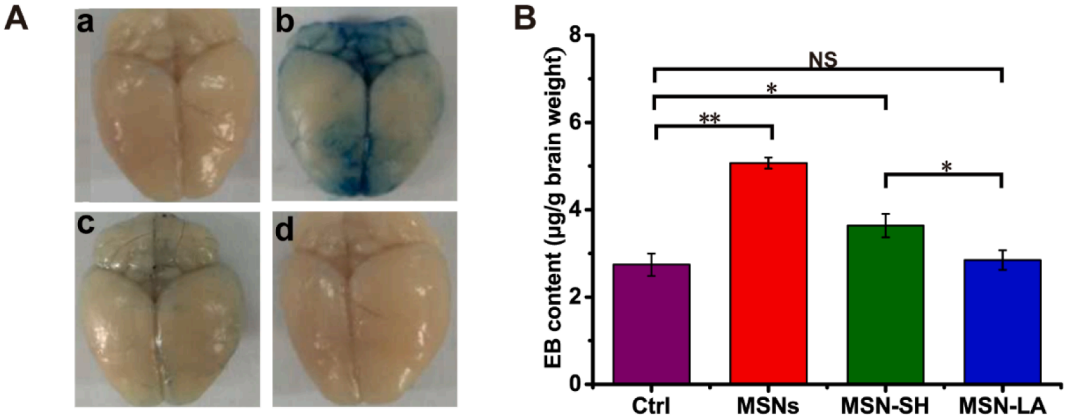


Fig. 9. (A) The gross view of the mice brain staining with EB. The blue color indicated the disruption of the BBB induced by the mesoporous silica. (B) The quantified Evans blue extravasation. (a) the control, (b) pristine MSNs, (c) MSN–SH, and (d) MSN–LA groups. NS, not significant, * $p < 0.05$, ** $p < 0.01$. (For interpretation of the references to color in this figure legend, the reader is referred to the web version of this article.)

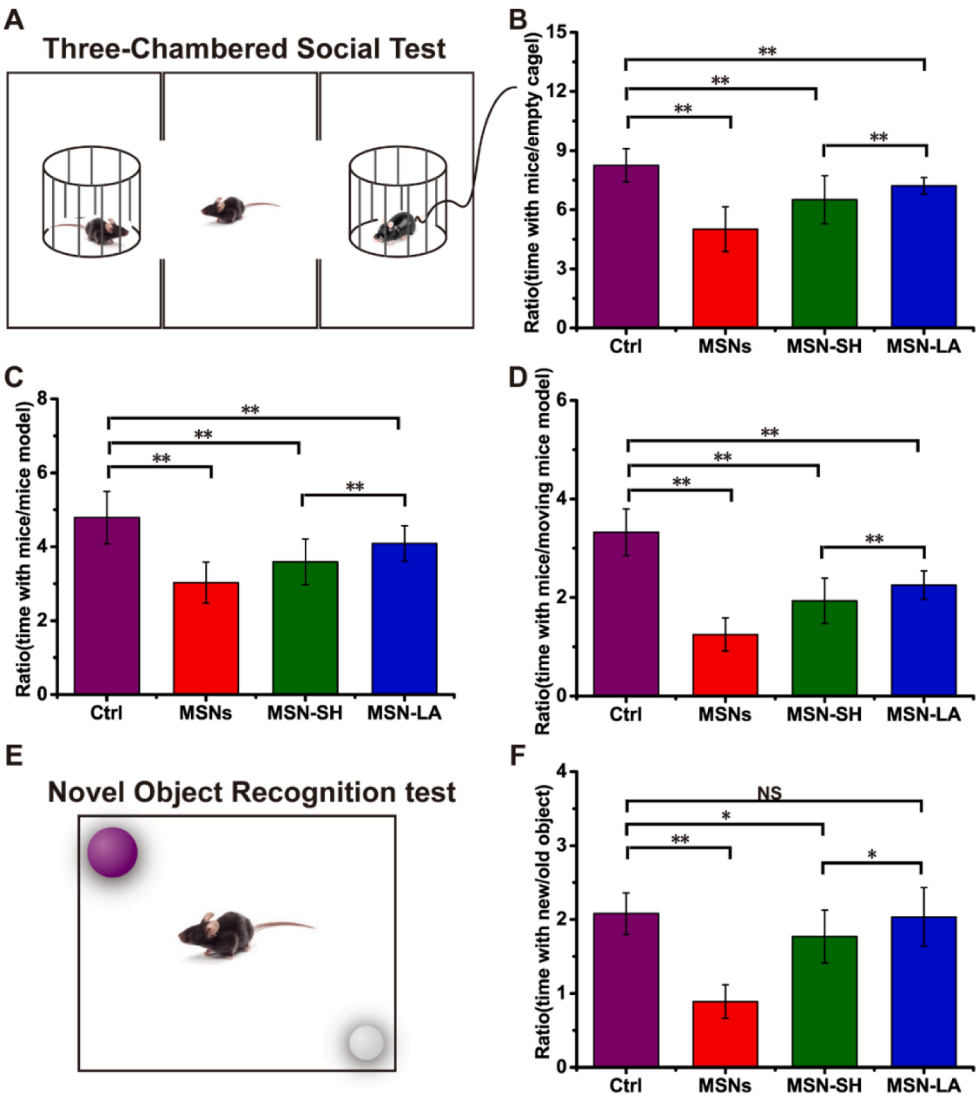


Fig. 10. Effects on social interaction and cognition in C57BL/6N mice after administration of the mesoporous silica. (A) The schematic diagram of three-chambered social test. (B) The social communication behavior of the mice with empty cages and strange mice, indicated with $R_{s/c}$. (C) The social communication behavior of the mice with the model mice and strange mice, indicated with $R_{s/m}$. (D) The social communication behavior of mice with movable model mice and strange mice, as indicated with $R_{s/mm}$. (E) The schematic diagram of novel object recognition test. (F) The novel object recognition ability, as indicated with $R_{n/o}$. $n = 8$, NS, not significant, * $p < 0.05$, ** $p < 0.01$.

mesoporous silica on the brain function, three-chambered social approach task and novel object recognition test were performed to evaluate the social communication ability and cognitive function of the mice at 8 weeks of age [77].

Mice exhibits a rich repertoire of social behaviors, which are important for forming bonds, foraging, defending territories, avoiding predators, and reproducing successfully [78]. They also have a natural tendency to approach and investigate unfamiliar conspecifics. The automated three-chambered social approach task was originally designed in 2004 and has been widely employed as a standard test to assess sociability in the mice [54,55]. Sociability is defined as the subject mouse spending more time in the chamber containing the novel mouse than in the chamber containing the inanimate novel object. In the three-chambered social test (Fig. 10**A**), the sociability of C57BL/6N mice was assessed via the social communication behavior of the mice with empty cage and strange mice, with model mouse and strange mouse, and with movable model mouse and strange mouse, and the result was corroboratively measured with time the mouse spent on sniffing the strange mice versus time spent in empty cage ($R_{s/c}$, Fig. 10**B**), time on strange mouse versus on model mouse ($R_{s/m}$, Fig. 10**C**), and time on strange mouse versus on movable model ($R_{s/mm}$, Fig. 10**D**). $R_{s/mm}$, $R_{s/c}$, and $R_{s/mm}$ are used to measure direct social interactions. The group administrated with 5% glucose was set as the control. Compared to the control, decline degree of $R_{s/c}$ (from 8.25 to 5.01), $R_{s/m}$(from 4.79 to 3.03), and $R_{s/mm}$ (from 3.33 to 1.25) is the most remarkable in the pristine MSNs treated group, suggesting the sociability significantly declined after the nanoparticle administration. There is also statistical difference between the control and the MSN–SH group ($R_{s/c}$ from 8.25 to 6.50, $R_{s/m}$ from 4.79 to 3.59, and $R_{s/mm}$ from 3.33 to 1.93), the control and the MSN–LA group ($R_{s/c}$ from 8.25 to 7.21, $R_{s/m}$ from 4.79 to 4.09, and $R_{s/mm}$ from 3.33 to 2.25). These data indicated that the mice in the pristine MSNs group showed the most significant decrease in social interaction activity compared to the control. Notably, declined social communication behavior and sociability dysfunction are common disorder observed in patients with neurodegeneration [79], implying the risk of behavior dysfunction and neurodegenerative diseases after exposure to the pristine MSNs. In the MSN–SH group, sociability dysfunction of the mice was alleviated as suggested by the rise of data $R_{s/mm}$, $R_{s/c}$, and $R_{s/mm}$ compared with that of the pristine MSNs group. The declined sociability was further minimized in the MSN–LA group, as indicated by the highest $R_{s/mm}$, $R_{s/c}$, and $R_{s/mm}$ among the treated mice. It suggested that antioxidative modification of the pristine MSNs is conducive to prevent from the sociability decline, and LA modification showed higher potency to protect the damage from the MSNs.

The cognitive function of the mice after treatment was assessed with a novel object recognition experiment (Fig. 10**E**). The result was corroboratively measured with time the mouse spent on sniffing the new object versus time spent on the old one ($R_{n/o}$, Fig. 10**F**). Consistent with

the sociability test, the mice after the pristine MSNs administration displayed the most severe cognitive impairment after 14 days of nanoparticles exposure, with $R_{n/o}$ from 2.08 (the control) to 0.89 (−1.34 fold, $p = 0.0000$), which was highlighted by their failure to recognize a novel object. The mice after MSN–SH administration showed a slight cognitive impairment, with $R_{n/o}$ declined only to 1.77 (−0.18 fold, $p = 0.0101$). Most interestingly, the mice administrated with MSN–LA displayed a comparable $R_{n/o}$ (2.03) to the control mice, suggesting that the cognitive function was not impaired, due to the protective effect of LA modification on the MSNs. Compared with the pristine MSNs, MSN–SH played a certain neuroprotective role with an improved cognitive outcome, while MSN–LA could almost avoid induce the damage on cognitive function of the mice.

Recent studies have implicated that deteriorated structure and function of the BBB, together with the other factors facilitating neuroinflammatory processes, may account for the neuronal loss, social activity disorders including depression and anxiety, and cognitive decline. In the present work, it is also noted that the behaviors disorder of the mice is correlated with the destruction of BBB induced by the MSNs. The pristine MSNs caused the severest destruction of BBB, and thus the most declined brain function was observed in the mice treated with the MSNs. Compared with the pristine MSNs, the antioxidative modification with both thiol and LA could mitigate the brain dysfunction caused by the MSNs administration, with LA playing the most prominent neuroprotective role.

4. Conclusion

We have fabricated a novel LA modified mesoporous silica MSN–LA, which could suppress the ROS generation induced by the MSNs, due to superior anti-oxidative property of LA. The pristine MSNs showed the highest generation of intracellular ROS, and induced the severest cytotoxicity *in vitro* and *in vivo*, which caused the most prominent brain damage, as reflected by the declined sociability and cognition of the mice. The molecular mechanism of cytotoxicity of the MSNs *in vitro* was revealed to result from mitochondria damage and suppressed energetic metabolism by the intracellular ROS, with apoptosis activated via MAPK signaling pathway. Modification of the pristine MSNs with anti-oxidative thiol or LA could alleviate significantly the cytotoxicity *in vitro* and *in vivo*. Most interestingly, MSN–LA showed the most trivial cytotoxicity and induced the slightest brain dysfunction, due to superior anti-oxidative ability of LA. It disclaimed the risk of the pristine MSNs applied in the drug delivery, especially, brain-targeted drug delivery. This study represents the first example of the brain function and behaviors influenced by the MSNs in live animals, and it is important because of the brain dysfunction observed. We believe the reduced *in vivo* toxicity of this potential nanomaterial via LA modification provides a promising pathway for clinical biomedical applications such as drug delivery and diagnosis.

Declaration of Competing Interest

The authors declare that they have no known competing financial interests or personal relationships that could have appeared to influence the work reported in this paper.

Acknowledgements

The authors thank the Natural Science Foundation of China (21571133, 21171120, 31801208, 91854209), Beijing Natural Science Foundation Program and Scientific Research Key Program of Beijing Municipal Commission of Education (KZ201710025024), and Natural Science Foundation of Beijing Municipality (7132020).

Appendix A. Supplementary data

Supplementary data to this article can be found online at https://doi.org/10.1016/j.cej.2021.128957.

References

[1] D. Tarn, C.E. Ashley, M. Xue, E.C. Carnes, J.I. Zink, C.J. Brinker, Mesoporous silica nanoparticle nanocarriers: biofunctionality and biocompatibility, Acc. Chem. Res. 46 (3) (2013) 792–801, https://doi.org/10.1021/ar3000986.
[2] Q.i. Lei, S.-B. Wang, J.-J. Hu, Y.-X. Lin, C.-H. Zhu, L. Rong, X.-Z. Zhang, Stimuli-responsive "cluster bomb" for programmed tumor therapy, ACS Nano 11 (7) (2017) 7201–7214, https://doi.org/10.1021/acsnano.7b0308810.1021/acsnano.7b03088.s001.
[3] C. Argyo, V. Weiss, C. Bräuchle, T. Bein, Multifunctional mesoporous silica nanoparticles as a universal platform for drug delivery, Chem. Mater. 26 (1) (2014) 435–451, https://doi.org/10.1021/cm402592t.
[4] F. Chen, H. Hong, Y. Zhang, H.F. Valdovinos, S. Shi, G.S. Kwon, C.P. Theuer, T. E. Barnhart, W. Cai, In vivo tumor targeting and image-guided drug delivery with antibody-conjugated, radio labeled mesoporous silica nanoparticles, ACS Nano 7 (10) (2013) 9027–9039, https://doi.org/10.1021/nn403617j.
[5] Y. Wang, H. Gu, Core-shell-type magnetic mesoporous silica nanocomposites for bioimaging and therapeutic agent delivery, Adv. Mater. 27 (3) (2015) 576–585, https://doi.org/10.1002/adma.v27.310.1002/adma.201401124.
[6] H. Meng, W.X. Mai, H. Zhang, M. Xue, T. Xia, S. Lin, X. Wang, Y. Zhao, Z. Ji, J. I. Zink, A.E. Nel, Codelivery of an optimal drug/siRNA combination using mesoporous silica nanoparticles to overcome drug resistance in breast cancer in vitro and in vivo, ACS Nano 7 (2) (2013) 994–1005, https://doi.org/10.1021/nn3044066.
[7] M. Wu, Q. Meng, Y.u. Chen, L. Zhang, M. Li, X. Cai, Y. Li, P. Yu, L. Zhang, J. Shi, Large pore-sized hollow mesoporous organosilica for redox-responsive gene delivery and synergistic cancer chemotherapy, Adv. Mater. 28 (10) (2016) 1963–1969, https://doi.org/10.1002/adma.201505524.
[8] W. Fan, N. Lu, P. Huang, Y.i. Liu, Z. Yang, S. Wang, G. Yu, Y. Liu, J. Hu, Q. He, J. Qu, T. Wang, X. Chen, Glucose-responsive sequential generation of hydrogen peroxide and nitric oxide for synergistic cancer starving-like/gas therapy, Angew. Chem. Int. Ed. 56 (5) (2017) 1229–1233, https://doi.org/10.1002/anie.201610682.
[9] J.M. Rosenholm, V. Mamaeva, C. Sahlgren, M. Linden, Nanoparticles in targeted cancer therapy: mesoporous silica nanoparticles entering preclinical development stage, Nanomedicine 7 (2012) 111–120, https://doi.org/10.2217/nnm.11.166.
[10] F. Lu, S.-H. Wu, Y. Hung, C.-Y. Mou, Size effect on cell uptake in well-suspended, uniform mesoporous silica nanoparticles, Small 5 (12) (2009) 1408–1413, https://doi.org/10.1002/smll.v5:1210.1002/smll.200900005.
[11] D. Breznan, D.D. Das, C. MacKinnon-Roy, S. Bernatchez, A. Sayari, M. Hill, R. Vincent, P. Kumarathasan, Physicochemical properties can be key determinants of mesoporous silica nanoparticle potency in vitro, ACS Nano 12 (12) (2018) 12062–12079, https://doi.org/10.1021/acsnano.8b0491010.1021/acsnano.8b04910.s00110.1021/acsnano.8b04910.s002.
[12] S.P. Hudson, R.F. Padera, R. Langer, D.S. Kohane, The biocompatibility of mesoporous silicates, Biomaterials 29 (30) (2008) 4045–4055, https://doi.org/10.1016/j.biomaterials.2008.07.007.
[13] T. Liu, L. Li, C. Fu, H. Liu, D. Chen, F. Tang, Pathological mechanisms of liver injury caused by continuous intraperitoneal injection of silica nanoparticles, Biomaterials 33 (7) (2012) 2399–2407, https://doi.org/10.1016/j.biomaterials.2011.12.008.
[14] T. Liu, L. Li, X.u. Teng, X. Huang, H. Liu, D. Chen, J. Ren, J. He, F. Tang, Single and repeated dose toxicity of mesoporous hollow silica nanoparticles in intravenously exposed mice, Biomaterials 32 (6) (2011) 1657–1668, https://doi.org/10.1016/j.biomaterials.2010.10.035.
[15] C. Fu, T. Liu, L. Li, H. Liu, D. Chen, F. Tang, The absorption, distribution, excretion and toxicity of mesoporous silica nanoparticles in mice following different exposure routes, Biomaterials 34 (10) (2013) 2565–2575, https://doi.org/10.1016/j.biomaterials.2012.12.043.
[16] C. Xi, Z. Wang, J. Zhou, X. Fu, J. Liang, Y. Qiu, Z. Huang, Renal interstitial fibrosis induced by high-dose mesoporous silica nanoparticles via the NF-κB signaling pathway, Int. J. Nanomed. 10 (2015) 1–22, https://doi.org/10.2147/IJN.S73538.
[17] Y.-S. Lin, C.L. Haynes, Impacts of mesoporous silica nanoparticle size, pore ordering, and pore integrity on hemolytic activity, J. Am. Chem. Soc. 132 (13) (2010) 4834–4842, https://doi.org/10.1021/ja910846q.
[18] W.G. Hozayen, A.M. Mahmoud, E.M. Desouky, E.-S. El-Nahass, H.A. Soliman, A. A. Farghali, Cardiac and pulmonary toxicity of mesoporous silica nanoparticles is associated with excessive ROS production and redox imbalance in Wistar rats, Biomed. Pharmacother. 109 (2019) 2527–2538, https://doi.org/10.1016/j.biopha.2018.11.093.
[19] C. Guo, J.i. Wang, L.i. Jing, R.u. Ma, X. Liu, L. Gao, L. Cao, J. Duan, X. Zhou, Y. Li, Z. Sun, Mitochondrial dysfunction, perturbations of mitochondrial dynamics and biogenesis involved in endothelial injury induced by silica nanoparticles, Environ. Pollut. 236 (2018) 926–936.
[20] J.-H. Park, L. Gu, G. von Maltzahn, E. Ruoslahti, S.N. Bhatia, M.J. Sailor, Biodegradable luminescent porous silicon nanoparticles for in vivo applications, Nat. Mater. 8 (4) (2009) 331–336, https://doi.org/10.1038/nmat2398.
[21] T. Nash, A.C. Allison, J.S. Harington, Physico-chemical properties of silica in relation to its toxicity, Nature 210 (5033) (1966) 259–261, https://doi.org/10.1038/210259a0.

[22] X. Liu, B. Sui, J. Sun, Blood-brain barrier dysfunction induced by silica NPs in vitro and in vivo: Involvement of oxidative stress and Rho-kinase/JNK signaling pathways, Biomaterials 121 (2017) 64–82, https://doi.org/10.1016/j.biomaterials.2017.01.006.
[23] M. Ott, V. Gogvadze, S. Orrenius, B. Zhivotovsky, Mitochondria, oxidative stress and cell death, Apoptosis 12 (5) (2007) 913–922, https://doi.org/10.1007/s10495-007-0756-2.
[24] M.J. Forster, A. Dubey, K.M. Dawson, W.A. Stutts, H. Lal, R.S. Sohal, Age-related losses of cognitive function and motor skills in mice are associated with oxidative protein damage in the brain, Proc. Natl. Acad. Sci. U. S. A. 93 (10) (1996) 4765–4769, https://doi.org/10.1073/pnas.93.10.4765.
[25] T. Dandekar, Free radicals and memory loss, Redox Rep. 3 (1) (1997) 71–73, https://doi.org/10.1080/13510002.1997.11747093.
[26] S. Saeidnia, M. Abdollahi, Toxicological and pharmacological concerns on oxidative stress and related diseases, Toxicol. Appl. Pharmacol. 273 (3) (2013) 442–455, https://doi.org/10.1016/j.taap.2013.09.031.
[27] M. Zhou, L. Xie, C.-J. Fang, H. Yang, Y.-J. Wang, X.-Y. Zhen, C.-H. Yan, Y. Wang, M. Zhao, S. Peng, Implications for blood-brain-barrier permeability, in vitro oxidative stress and neurotoxicity potential induced by mesoporous silica nanoparticles: effects of surface modification, RSC Adv. 6 (2016) 2800–2809, https://doi.org/10.1039/c5ra17517h.
[28] L. Packer, E.H. Witt, H.J. Tritschler, Alpha-Lipoic acid as a biological antioxidant, Free Radic. Biol. Med. 19 (2) (1995) 227–250, https://doi.org/10.1016/0891-5849(95)00017-R.
[29] G.P. Biewenga, G.R.M.M. Haenen, A. Bast, The pharmacology of the antioxidant lipoic acid, Gen. Pharmacol. 29 (3) (1997) 315–331, https://doi.org/10.1016/S0306-3623(96)00474-0.
[30] J.H. Suh, S.V. Shenvi, B.M. Dixon, H. Liu, A.K. Jaiswal, R.-M. Liu, T.M. Hagen, Decline in transcriptional activity of Nrf2 causes age-related loss of glutathione synthesis, which is reversible with lipoic acid, Proc. Natl. Acad. Sci. U. S. A. 101 (10) (2004) 3381–3386, https://doi.org/10.1073/pnas.0400282101.
[31] S.H. Ki, S.G. Kim, Phase II enzyme induction by alpha-lipoic acid through phosphatidylinositol 3-kinase-dependent C/EBPs activation, Xenobiotica 38 (2008) 587–604, https://doi.org/10.1080/00498250802126920.
[32] L. Rochette, S. Ghibu, C. Richard, M. Zeller, Y. Cottin, C. Vergely, Direct and indirect antioxidant properties of α-lipoic acid and therapeutic potential, Mol. Nutr. Food Res. 57 (1) (2013) 114–125, https://doi.org/10.1002/mnfr.201200608.
[33] B. Doersam, J. Fahrer, The disulfide compound α-lipoic acid and its derivatives: A novel class of anticancer agents targeting mitochondria, Cancer Lett. 371 (2016) 12–19, https://doi.org/10.1016/j.canlet.2015.11.019.
[34] D. Han, G. Handelman, L. Marcocci, C.K. Sen, S. Roy, H. Kobuchi, H.J. Tritschler, L. Flohé, L. Packer, Lipoic acid increases de novo synthesis of cellular glutathione by improving cystine utilization, Biofactors 6 (3) (1997) 321–338, https://doi.org/10.1002/biof.v6:310.1002/biof.5520060303.
[35] A. Lahiani, A. Hidmi, J. Katzhendler, E. Yavin, P. Lazarovici, Novel synthetic pegylated conjugate of α-lipoic acid and tempol reduces cell death in a neuronal PC12 clonal line subjected to ischemia, ACS Chem. Neurosci. 7 (10) (2016) 1452–1462, https://doi.org/10.1021/acschemneuro.6b00211.
[36] S. Paradells-Navarro, M.S. Benlloch-Navarro, M.I. Almansa Frias, M.A. Garcia-Esparza, V. Broccoli, M. Miranda, J.M. Soria, Neuroprotection of brain cells by lipoic acid treatment after cellular stress, ACS Chem. Neurosci. 8 (3) (2017) 569–577, https://doi.org/10.1021/acschemneuro.6b00306.
[37] L. Packer, H.J. Tritschler, K. Wessel, Neuroprotection by the metabolic antioxidant α-lipoic acid, Free Radic. Biol. Med. 22 (1-2) (1997) 359–378, https://doi.org/10.1016/S0891-5849(96)00269-9.
[38] B. Shukitt–Hale, D.E. Smith, M. Meydani, J.A. Joseph, The effects of dietary antioxidants on psychomotor performance in aged mice, Exp. Gerontol. 34 (6) (1999) 797–808, https://doi.org/10.1016/S0531-5565(99)00039-X.
[39] J.K. Liu, E. Head, A.M. Gharib, W.J. Yuan, R.T. Ingersoll, T.M. Hagen, C. W. Cotman, B.N. Ames, Memory loss in old rats is associated with brain mitochondrial decay and RNA/DNA oxidation: Partial reversal by feeding acetyl-L-carnitine and/or R-α-lipoic acid, Proc. Natl. Acad. Sci. U. S. A. 99 (2002) 2356–2361, https://doi.org/10.1073/pnas.261709299.
[40] S.A. Farr, H.F. Poon, D. Dogrukol-Ak, J. Drake, W.A. Banks, E. Eyerman, D. A. Butterfield, J.E. Morley, The antioxidants alpha-lipoic acid and N-acetylcysteine reverse memory impairment and brain oxidative stress in aged SAMP8 mice, J. Neurochem. 84 (2003) 1173–1183, https://doi.org/10.1046/j.1471-4159.2003.01580.x.
[41] M. Sharma, Y.K. Gupta, Effect of alpha lipoic acid on intracerebroventricular streptozotocin model of cognitive impairment in rats, Eur. Neuropsychopharmacol. 13 (4) (2003) 241–247, https://doi.org/10.1016/S0924-977X(03)00008-7.
[42] J.F. Quinn, J.R. Bussiere, R.S. Hammond, T.J. Montine, E. Henson, R.E. Jones, R. W. Stackman, Chronic dietary α-lipoic acid reduces deficits in hippocampal memory of aged Tg2576 mice, Neurobiol. Aging 28 (2) (2007) 213–225, https://doi.org/10.1016/j.neurobiolaging.2005.12.014.
[43] S.A. Farr, T.O. Price, W.A. Banks, N. Ercal, J.E. Morley, Effect of alpha-lipoic acid on memory, oxidation, and lifespan in samp8 mice, J. Alzheimer's Dis. 32 (2) (2012) 447–455, https://doi.org/10.3233/JAD-2012-120130.
[44] A. Mahboob, S.M. Farhat, G. Iqbal, M.M. Babar, N.-u.-S. Zaidi, S.M. Nabavi, T. Ahmed, Alpha-lipoic acid-mediated activation of muscarinic receptors improves hippocampus- and amygdala-dependent memory, Brain Res. Bull. 122 (2016) 19–28, https://doi.org/10.1016/j.brainresbull.2016.02.014.
[45] Z. Meng, Y. Liu, X. Li, Z. Ma, Removal of siloxane (L2) from biogas using methyl-functionalised silica gel as adsorbent, Chem. Eng. J. 389 (2020), https://doi.org/10.1016/j.cej.2020.124440.
[46] S. Chen, F. Zi, X. Hu, Y. Chen, P. Yang, Q. Wang, X. Qin, H. Cheng, Y. Liu, Y. He, C. Wang, D. Hu, Y. Liu, Y. Zhang, Interfacial properties of mercaptopropyl-functionalised silica gel and its adsorption performance in the recovery of gold(I) thiosulfate complex, Chem. Eng. J. 393 (2020), https://doi.org/10.1016/j.cej.2020.124547.
[47] S.L. Burkett, S.D. Sims, S. Mann, Synthesis of hybrid inorganic-organic mesoporous silica by co-condensation of siloxane and organosiloxane precursors, Chem. Commun. 11 (1996) 1367–1368, https://doi.org/10.1039/CC9960001367.
[48] S. Huh, J.W. Wiench, J.C. Yoo, M. Pruski, V.S.Y. Lin, Organic functionalization and morphology control of mesoporous silicas via a co-condensation synthesis method, Chem. Mater. 22 (2003) 4247–4256, https://doi.org/10.1021/cm0210041.
[49] Y.S. Lin, C.L. Haynes, Synthesis and characterization of biocompatible and size-tunable multifunctional porous silica nanoparticles, Chem. Mater. 17 (2009) 3979–3986, https://doi.org/10.1021/cm901259n.
[50] A. Cauvel, G. Renard, D. Brunel, Monoglyceride synthesis by heterogeneous catalysis using mcm-41 type silicas functionalized with amino groups, J. Org. Chem. 3 (1997) 749–751, https://doi.org/10.1021/jo9614001.
[51] N. Zhan, G. Palui, M. Safi, X. Ji, H. Mattoussi, Multidentate zwitterionic ligands provide compact and highly biocompatible quantum dots, J. Am. Chem. Soc. 37 (2013) 13786–13795, https://doi.org/10.1021/ja405010v.
[52] K.H. Shim, K.-H. Jeong, S.O. Bae, M.O. Kang, E.H. Maeng, C.S. Choi, Y.-R. Kim, J. Hulme, E.K. Lee, M.-K. Kim, S.S.A. An, Assessment of ZnO and SiO_2 nanoparticle permeability through and toxicity to the blood-brain barrier using Evans blue and TEM, Int. J. Nanomed. 9 (2014) 225–233, https://doi.org/10.2147/IJN.S58205.
[53] J. Sullivan-Brown, M.E. Bisher, R.D. Burdine, Embedding, serial sectioning and staining of zebrafish embryos using JB-4 resin, Nat. Protoc. 6 (1) (2011) 46–55, https://doi.org/10.1038/nprot.2010.165.
[54] M. Yang, J.L. Silverman, J.N. Crawley, Automated three-chambered social approach task for mice, Curr. Protoc. Neurosci. 8 (2011) Unit 8.26-Unit 28.26, 10.1002/0471142301.ns0826s56.
[55] J.J. Nadler, S.S. Moy, G. Dold, D. Trang, N. Simmons, A. Perez, N.B. Young, R. P. Barbaro, J. Piven, T.R. Magnuson, J.N. Crawley, Automated apparatus for quantitation of social approach behaviors in mice, Genes Brain Behav. 3 (2004) 303–314, https://doi.org/10.1111/j.1601-183X.2004.00071.x.
[56] H.-R. Xie, L.-S. Hu, G.-Y. Li, SH-SY5Y human neuroblastoma cell line: in vitro cell model of dopaminergic neurons in Parkinson's disease, Chin. Med. J. 123 (2010) 1086–1092, https://doi.org/10.3760/cma.j.issn.0366-6999.2010.08.021.
[57] S. Amini, M.K. White, S. Amini, M.K. White, Methods in molecular biology, neuronal cell culture, methods and protocols 1078 (2013), https://doi.org/10.1007/978-1-62703-640-5.
[58] E.E. Battin, J.L. Brumaghim, Metal specificity in DNA damage prevention by sulfur antioxidants, J. Inorg. Biochem. 102 (12) (2008) 2036–2042, https://doi.org/10.1016/j.jinorgbio.2008.06.010.
[59] C. Li, K.-W. Ip, W.-L. Man, D. Song, M.-L. He, S.-M. Yiu, T.-C. Lau, G. Zhu, Cytotoxic (salen) ruthenium(III) anticancer complexes exhibit different modes of cell death directed by axial ligands, Chem. Sci. 8 (2017) 6865–6870, https://doi.org/10.1039/c7sc02205k.
[60] E.F. Korman, G.A. Blondin, W.J. Vail, D.E. Green, The mechanism of mitochondrial swelling. VII. The constant topology of the mitochondrial inner membrane during swelling, J. Bioenerg. 1 (4) (1970) 379–386, https://doi.org/10.1007/BF01654575.
[61] W.H. Gao, Y.M. Pu, K.Q. Luo, D.C. Chang, Temporal relationship between cytochrome c release and mitochondrial swelling during UV-induced apoptosis in living HeLa cells, J. Cell Sci. 114 (2001) 2855–2862, https://doi.org/10.1023/A:1010615508916.
[62] B.G. Hill, B.P. Dranka, L. Zou, J.C. Chatham, V.M. Darley-Usmar, Importance of the bioenergetic reserve capacity in response to cardiomyocyte stress induced by 4-hydroxynonenal, Biochem. J. 424 (2009) 99–107, https://doi.org/10.1042/BJ20090934.
[63] M. Wu, A. Neilson, A.L. Swift, R. Moran, J. Tamagnine, D. Parslow, S. Armistead, K. Lemire, J. Orrell, J. Teich, S. Chomicz, D.A. Ferrick, Multiparameter metabolic analysis reveals a close link between attenuated mitochondrial bioenergetic function and enhanced glycolysis dependency in human tumor cells, Am. J. Physiol.- Cell Physiol. 292 (1) (2007) C125–C136, https://doi.org/10.1152/ajpcell.00247.2006.
[64] D.A. Ferrick, A. Neilson, C. Beeson, Advances in measuring cellular bioenergetics using extracellular flux, Drug Discovery Today 13 (5-6) (2008) 268–274, https://doi.org/10.1016/j.drudis.2007.12.008.
[65] S.A. Susin, H.K. Lorenzo, N. Zamzami, I. Marzo, B.E. Snow, G.M. Brothers, J. Mangion, E. Jacotot, P. Costantini, M. Loeffler, N. Larochette, D.R. Goodlett, R. Aebersold, D.P. Siderovski, J.M. Penninger, G. Kroemer, Molecular characterization of mitochondrial apoptosis-inducing factor, Nature 397 (6718) (1999) 441–446, https://doi.org/10.1038/17135.
[66] M.R. Junttila, S.-P. Li, J. Westermarck, Phosphatase-mediated crosstalk between MAPK signalling pathways in the regulation of cell survival, FASEB J. 22 (2008) 954–965, https://doi.org/10.1096/fj.06-7859rev.
[67] G.L. Johnson, R. Lapadat, Mitogen-activated protein kinase pathways mediated by ERK, JNK, and p38 protein kinases, Science 298 (2002) 1911–1912, https://doi.org/10.1126/science.1072682.
[68] Y. Son, S. Kim, H.-T. Chung, H.-O. Pae, Reactive oxygen species in the activation of map kinases, Methods Enzymol 528 (2013) 27–48, https://doi.org/10.1016/B978-0-12-405881-1.00002-1.
[69] Y. Huang, L. He, W. Liu, C. Fan, W. Zheng, Y.-S. Wong, T. Chen, Selective cellular uptake and induction of apoptosis of cancer-targeted selenium nanoparticles, Biomaterials 34 (29) (2013) 7106–7116, https://doi.org/10.1016/j.biomaterials.2013.04.067.

[70] S. Wang, X. Ren, X. Hu, L. Zhou, C. Zhang, M. Zhang, Cadmium-induced apoptosis through reactive oxygen species-mediated mitochondrial oxidative stress and the JNK signaling pathway in TM_3 cells, a model of mouse Leydig cells, Toxicol. Appl. Pharmacol. 368 (2019) 37–48, https://doi.org/10.1016/j.taap.2019.02.012.
[71] A. Guerra-Castellano, A. Díaz-Quintana, G. Pérez-Mejías, C.A. Elena-Real, K. González-Arzola, S.M. García-Mauriño, M.A. De la Rosa, I. Díaz-Moreno, Oxidative stress is tightly regulated by cytochrome c phosphorylation and respirasome factors in mitochondria, Proc. Natl. Acad. Sci. U. S. A. 115 (31) (2018) 7955–7960, https://doi.org/10.1073/pnas.1806833115.
[72] D.R. Green, J.C. Reed, Mitochondria and apoptosis, Science 281 (1998) 1309–1312, https://doi.org/10.1046/j.1432-1327.1998.2520001.x.
[73] P. Li, D. Nijhawan, I. Budihardjo, S.M. Srinivasula, M. Ahmad, E.S. Alnemri, X. Wang, Cytochrome c and dATP-dependent formation of Apaf-1/caspase-9 complex initiates an apoptotic protease cascade, Cell 91 (4) (1997) 479–489, https://doi.org/10.1016/S0092-8674(00)80434-1.
[74] M.O. Hengartner, The biochemistry of apoptosis, Nature 407 (6805) (2000) 770–776, https://doi.org/10.1038/35037710.
[75] S.I. Rapoport, Osmotic opening of the blood-brain barrier: Principles, mechanism, and therapeutic applications, Cell. Mol. Neurobiol. 20 (2000) 217–230, https://doi.org/10.1023/A:1007049806660.
[76] S.D. Kong, J. Lee, S. Ramachandran, B.P. Eliceiri, V.I. Shubayev, R. Lal, S. Jin, Magnetic targeting of nanoparticles across the intact blood-brain barrier, J. Controlled Release 164 (1) (2012) 49–57, https://doi.org/10.1016/j.jconrel.2012.09.021.
[77] R. Daneman, The blood-brain barrier in health and disease, Ann. Neurol. 72 (5) (2012) 648–672, https://doi.org/10.1002/ana.v72.510.1002/ana.23648.
[78] C. Sue Carter, Neuroendocrine perspectives on social attachment and love, Psychoneuroendocrinology 23 (8) (1998) 779–818, https://doi.org/10.1016/S0306-4530(98)00055-9.
[79] J.L. Cummings, C. Diaz, M. Levy, G. Binetti, I.I. Litvan, Neuropsychiatric syndromes in neurodegenerative disease: frequency and signficance, Semin. Clin. Neuropsychiatry 1 (1996) 241–247, https://doi.org/10.1053/SCNP00100241.